International Journal of Mechanical Sciences xxx (xxxx) 106676

Contents lists available at ScienceDirect

International Journal of Mechanical Sciences

journal homepage: www.elsevier.com/locate/ijmecsci

Numerical investigation of the interaction of highly nonlinear solitary waves with corroded steel plates

Hoda Jalali, Piervincenzo Rizzo *

Laboratory for Nondestructive Evaluation and Structural Health Monitoring Studies, Department of Civil and Environmental Engineering, University of Pittsburgh, Pittsburgh, PA 15261, USA

ARTICLE INFO

Keywords:
Granular media
Non-destructive testing
Solitary waves
Finite element
Discrete element
Numerical methods

ABSTRACT

Over the last decade, a novel nondestructive evaluation (NDE) method based on the application of highly nonlinear solitary waves has emerged. The method is based on the actuation and detection of solitary waves propagating along a medium made of uniform spherical particles, the last of which is in contact with the material to be assessed noninvasively. The hypothesis is that the dynamic interaction between the wave and the material/structure to be inspected is dependent upon the condition of the material/structure. The study presented in this paper aims at designing and developing the NDE framework for the detection of localized corrosion in metals. In particular, this paper presents a numerical investigation of the interaction of highly nonlinear solitary waves with plates in pristine and corroded conditions. A coupled discrete/finite element model is used to predict the time of flight and the relative amplitudes of the reflected solitary waves as localized corrosion progresses in the plate. The sensitivity of the method is quantified in terms of different parameters such as plate thickness, chain length, and particles' mechanical and geometric properties. It is found that the sensitivity, i.e. the ability to detect corrosion at earlier stages, of this novel NDE technique is inversely proportional to the plate thickness and is proportional to the diameter and the stiffness of the particles. In the future, the findings of this study can be used to optimize the design of solitary wave transducers, which are devices that can be used to trigger, sustain, and detect the propagation of the solitary waves and their interaction with the structure of interest.

1. Introduction

Over the last decade, a novel nondestructive evaluation (NDE) and structural health monitoring (SHM) method based on highly nonlinear solitary waves has emerged as a low-cost, fast, and simple technique for the local inspection/monitoring of different materials and structures. Highly nonlinear solitary waves (HNSWs) are compact waves that have found many applications in physics and engineering including shock absorption, acoustic lensing, and energy harvesting [1-15], just to mention a few. In NDE and SHM applications, a short granular chain made of spherical particles is in point-contact with the structure to be inspected or monitored. A solitary wave, hereinafter referred to as the incident solitary wave (ISW), is induced at one end, propagates along the chain, and reaches the structure. Here, owing to principles discussed in this paper, the ISW reflects back giving rise to one or two solitary waves, the primary and the secondary reflected waves (PSW and SSW). Many studies have found that the amplitude and time of flight (ToF) of these reflected pulses are dependent on the mechanical and geometric characteristics of the structure [16-36].

The propagation of HNSWs in granular chains was first studied by Nesterenko [37,38], who showed numerically, analytically, and experimentally that uncompressed or lightly compressed 1D granular chains made of identical spherical particles support the generation and propagation of these waves. HNSWs present unique properties compared to linear waves propagating in continuous materials. For example, they support a high level of acoustic energy within a finite wavelength of five-particle diameters [39,40]. Moreover, their speed v_m can be tuned by changing the system's parameters like material properties [41-43], particles' shape and dimension [41-48], particles' configuration and arrangement [42,43,49], and initial static compression [40,50]. One of the distinctive features of HNSWs with respect to conventional acoustic waves is that their amplitude, characterized by the dynamic force F_m, is proportional to the wave speed, i.e. $F_m \alpha v_m^{6/5}$ [17,40].

Many groups have proven the feasibility of HNSWs in the field of NDE and SHM. Yang *et al.* [17] conducted a numerical, analytical, and

* Corresponding author.
E-mail address: pir3@pitt.edu (P. Rizzo).

https://doi.org/10.1016/j.ijmecsci.2021.106676
Received 17 January 2021; Received in revised form 26 June 2021; Accepted 14 July 2021
0020-7403/

experimental study to demonstrate that the amplitude and the delay of the reflected HSNWs at the interface of a large thin plate depend on the particles size, the plate thickness, and the distance of the interaction point from the plate boundaries. Cai *et al.* studied the interaction of HNSWs with a slender beam and reported that the reflected solitary waves features depend on the geometry and the mechanical properties of the beam and the thermal stress applied to the beam [18]. Kim *et al.* showed numerically and experimentally that the reflected solitary waves at the interface of a composite plate are sensitive to delamination in the composite plates [19]. Furthermore, numerical investigation of the interaction of HNSWs with composite beams showed that HNSWs are effective to evaluate the directional elastic properties of composite materials [20]. Other researchers demonstrated that the HNSW-based NDE method can be used for detecting subsurface voids [21], monitoring concrete hydration [22], assessing the quality of adhesive joints [23,24], examining the elastic properties and detecting delamination in composites [19,20,25-27,51], assessing the quality of orthopedic and dental implants [28,30,52], measuring the internal pressure of tennis balls [32,53,54], and quantifying axial stress [35,55]. Most of the above experimental studies are based on the use of "HNSW-transducers". The term is used here to indicate a mechanical device able to trigger, sustain, and sense solitary waves. The device consists of a 1-D chain of spherical particles; a frame holding the particles, an actuation system able to trigger single solitary pulses, and a sensor embedded in the chain to measure the waves.

Recently, the authors applied the HNSW-based NDE method to detect the onset of localized corrosion in a steel plate [36]. It was shown experimentally that the amplitude and the time of flight of the waves reflected at the interface between the chain and the plate are dependent on the presence of corrosion. The study was followed by the development of a wireless HNSW transducer that one day may enable the remote continuous implementation of the methodology [56].

The study presented in this paper expands the work in [36] by examining the effects of parameters such as size, number, and material of the particles on the sensitivity of the proposed method at detecting the onset and growth of localized corrosion. The scope of the study is to identify the optimal parameters of the HNSW transducer to maximize the sensitivity of the NDE method. The long-term objective of the study is to design HNSW transducers that are applicable at high temperature or radioactive environments where piezoelectric based ultrasonic testing cannot be implemented. This is especially important for petrochemical industries and power plants, where localized corrosion in pipelines is reported to be a significant contributing factor in accidents like leakage and explosion, and conventional NDE techniques like ultrasonic testing are limited by temperatures.

As described in [57], the most used corrosion monitoring techniques include linear polarization resistance (LPR) measurements, weight measurements and tactile metrological examinations. These techniques are, however, quite challenging as they require physical contact with either the electrolytes or the components of interest. Also, the conversion of LPR and weight measurements to wall losses depends on a number of assumptions. The use of ultrasonic testing is the best truly non-invasive method to measure thicknesses directly. The principle of ultrasonic testing is rather simple. High-frequency (typically 5 MHz or higher) bulk waves are sent into the wall and the thickness is estimated by extracting the temporal separation of the ultrasonic wave-packets that bounce up and down in the material whose thickness is being measured. Usually, a simple algorithm such as the timing between consecutive peaks is used to evaluate the travel time and hence the wall thickness [58]. A recent development [59] makes use of a waveguide-buffer that separates the high-temperature measurement area from the ultrasonic transducer and processing electronics. The system, commercialized by Permasense, uses two thin and long rectangular cross-section waveguides to isolate the vulnerable transducer and piezoelectric elements from the high-temperature measurement zone. The waveguides allow large temperature gradients to be sustained over short distances without the need for additional cooling equipment. When monitoring pipelines and plates, the use of guided ultrasonic waves (GUWs) that propagate along the pipes instead through the thickness is quite popular and effective because GUWs have many advantages with respect to the use of bulk through-thickness waves owing to the ability to inspect/monitor large areas from a single or a few positions, and therefore they do not provide local information of the pipe of interest [60-64]. However, GUW may not be suitable for pipes operating at high temperature owing to the Curie temperature affecting the piezoelectric elements.

This paper is organized as follows: Section 2 presents the numerical and the analytical methods implemented to study the interaction of HNSWs with plates in the pristine and corroded conditions. Section 3 presents the numerical and analytical predictions on the effect of different parameters like initial plate thickness, particle size, particle material properties, and chain length on the reflected solitary wave features. Finally, the paper concludes with a summary of the main conclusions drawn from the presented work in section 4.

2. Modeling

2.1. Coupled discrete / finite element modeling

The interaction of HNSWs with pristine and corroded plates was investigated using a discrete element (DE) model combined with a finite element (FE) analysis according to the scheme in Fig. 1. The DE model simulated the propagation of the solitary waves along the chain of particles whereas the FE model simulated the dynamic interaction between the particle in contact with the plate and the plate itself. The chain consisted of nine particles in order to be able to compare (see a later section of the paper) the results of this study with the results of some experiments conducted previously and published by the authors in [36]. The first eight particles, m_1-m_8, of the chain were modeled as a series of point masses connected with nonlinear axial springs and linear dampers (Fig. 1b). The nonlinear springs identify the Hertzian contact law (Fig. 1c):

$$F = A\delta_+^{3/2} \tag{1}$$

governing the mechanical interaction between adjacent particles. According to Eq. (1), the contact force F between two adjacent particles is nonlinearly proportional to the deformation δ of the diameter connecting the centers of the interacting particles. The subscript + denotes the operator max (δ, 0), which implies that there is no tensile force between the particles as they are separated from each other. For a chain composed of identical spherical particles, the contact stiffness coefficient A in Eq. (1) is equal to [65]:

$$A = \frac{E\sqrt{2R}}{3\left(1-\nu^2\right)} \tag{2}$$

where R, E, and ν are particles' radius, Young's modulus, and Poisson' ratio, respectively. Energy dissipation in the chain was simulated using linear dampers. The linear damping coefficient was equal to 4.5 N.s.m^{-1} as proposed by previous studies [16].

Both the last particle and the plate were modeled as deformable solids made of linear elastic material with no material damping. The plate was assumed simply supported along the edges. Owing to the symmetry in the geometry and loadings of the setup, a symmetric behavior was assumed in the setup. In fact, the system is symmetric around the xz and yz planes passing through the interaction point between the chain and the plate. Therefore, only a one-quarter of the geometry was simulated, and symmetry boundary conditions were applied to the planes of symmetry. Concentrated loads equal to one-quarter of the weight of the particles were applied on the mass points,

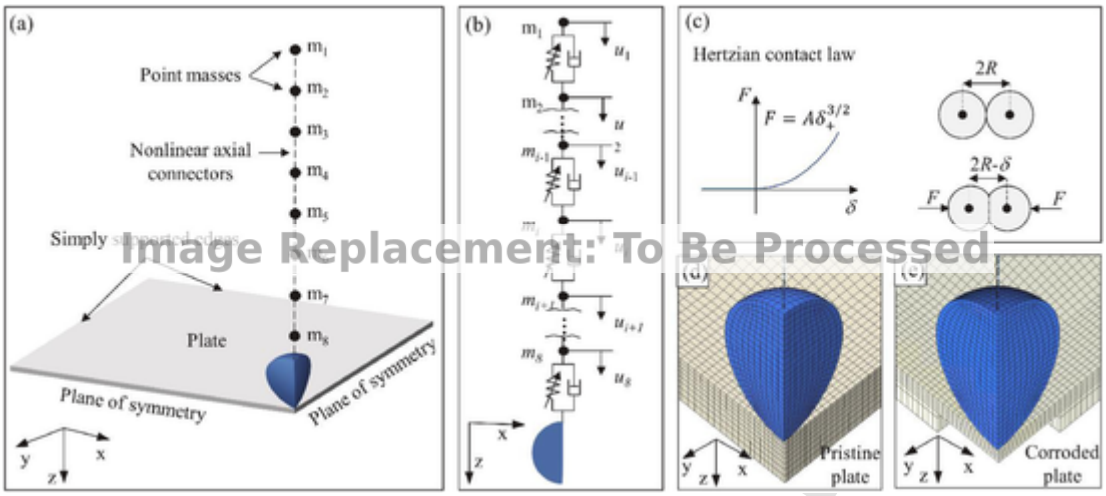

Fig. 1. Scheme of the analytical and numerical model. (a). The coupled discrete element (DE) and finite element (FE) model used in this study. One-quarter of the model is stimulated due to symmetry. (b) The DE model simulating the chain of particles as a spring-mass system, in which the point masses are connected by the nonlinear springs (defined based on the Hertzian contact law) and dashpots. (c) Graphical representation of the Hertzian contact law. The contact force between adjacent particles F is nonlinearly proportional to the deformation δ of the diameter connecting the centers of the interacting particles. (d) and (e) Zoom-in views of the FE model at the interface between the last particle and the plate in (d) pristine and (e) corroded conditions. Corrosion was simulated as a local thickness reduction in the plate, below the interaction point.

resulting in an initial static compression in the chain. Moreover, body forces were applied to model the effect of gravity.

The contact between the last particle and the plate was modeled using the hard contact interaction with frictionless tangential behavior. The mesh consisted of 3D 8-node linear isoparametric elements (C3D8 in Abaqus). The mesh size decreased gradually near the interface of the particle and the plate to improve the accuracy of deformations and stresses calculated at the interface (Fig. 1d and e).The mesh size was 0.4 mm in areas close the chain-plate interaction, and a preliminary mesh sensitivity analysis showed that further mesh refinement (e.g. using an element size of 0.2 mm close to the interaction area) does not change the properties of the solitary waves and the plate deformations significantly. The DE model was coupled to the FE model by connecting the nonlinear axial connector to the topmost node of the particle in the FE analysis.

The generation of the waves was simulated by applying an initial velocity of 0.31 m/s to the first particle (m_1) in the chain. This initial velocity is equivalent to the falling of the striker from a height of 5 mm in the previous experimental studies by the authors [36]. Localized corrosion was simulated as a local thickness reduction (mass loss) in a finite area (Fig. 1e). This modeling approach is based on the previous experimental observations by the authors [36] and other research studies in which localized corrosion was simulated by machining holes of different sizes and depths in plates and pipes [66-68]. The localized corrosion defects were 25.4 mm × 25.4 mm, positioned below the chain-plate interaction point, and the defect depth varied from 0 to 80 percent of the initial plate thickness. The interaction of HNSWs with the plate in pristine (Fig. 1d) and corroded (Fig. 1e) conditions was solved using Abaqus\Standard based on an implicit numerical algorithm. In each case, the time history of the displacement of the mass points and different nodes in the FE parts were extracted and analyzed for the effect of localized corrosion on the interaction between HNSWs and plates.

2.2. Analytical modeling

The time of flight and the normalized amplitude of the reflected solitary waves at the chain-plate interface of a thin plate were also predicted analytically by using the Zener model, which describes the normal impact of a single spherical particle on a large thin plate [69]. In this model it is assumed that the impact is over before the flexural waves are reflected from the boundaries. In fact, the model assumes that the duration of the impact between the plate and the interacting particle is so short that the reflected flexural waves from the plate boundaries may be neglected. It should be noted that this analytical model is more reliable in thick plates where the local contact stresses in the plate are not disturbed by the plate boundaries. The Zener model combines the equations of motion of the plate and the particle, yielding to the following nonlinear differential equation:

$$\left.\begin{array}{l} \frac{d^2\sigma}{d\tau^2} + \left(1 + \lambda\frac{d}{d\tau}\right)\sigma^{\frac{3}{2}} = 0 \\ \sigma = 0 \\ d\sigma/d\tau = 1 \end{array}\right\} \text{at } \tau = 0 \tag{3}$$

where τ is the dimensionless time, σ represents the dimensionless approach, and λ is a dimensionless inelasticity parameter that accounts for the energy dissipation during the impact, and defined as:

$$\lambda = \frac{\pi^{3/5}}{4\sqrt{3}} \left(\frac{2R}{h}\right)^2 \left(\frac{\rho b}{\rho p}\right)^{3/5} \left[\frac{v_m^2 \rho_p \left(1 - v_p^2\right)}{E_p}\right]^{1/10} \left[1 + \frac{E_p\left(1 - v_b^2\right)}{E_b\left(1 - v_p^2\right)}\right]^{-2/5} \tag{4}$$

In Eq. (4) h is the plate thickness, ρ is the density, and the subscripts b and p denote the bead and the plate, respectively.

In the analysis of the impact of a ball on a plate, the coefficient of restitution e identifies the ratio of the reflected to the impact velocity. This coefficient can be obtained as a function of λ by solving Eq. (3). Boettcher *et al.* proposed the following analytical approximation equation for the coefficient of restitution [70]:

$$e = \exp\left(-\pi\left(0.54975\lambda - 0.08507\lambda^2 + 0.08559\lambda^3 - 0.01163\lambda^4\right)\right) \tag{5}$$

When the plate thickness is much larger than the particle diameter ($h >> 2R$) or the plate is considerably stiffer than the bead ($E_p >> E_b$), the inelasticity parameter is nearly zero ($\lambda \approx 0$) and the restitution factor approaches one ($e \approx 1$). This implies that the particle does not lose kinematic energy during the impact due to the propagation of stress

waves in the plate, i.e. the plate behaves like a rigid body. During an inelastic impact ($\lambda > 0$), part of the kinematic energy of the particle is transferred to the plate ($e < 1$), causing flexural elastic waves propagating radially in the plate.

Owing to the relationship between amplitude and speed of the HNSWs $\left(F_m \alpha v_m^{6/5}\right)$, the coefficient of restitution e can be associated with the normalized amplitude (AR) of the solitary waves, defined as ratio of the amplitude of PSW to the amplitude of the ISW, as follows:

$$AR = \frac{F_{m,PSW}}{F_{m,ISW}} = \left(\frac{v_{\mathrm{m,PSW}}}{v_{\mathrm{m,ISW}}}\right)^{6/5} = e^{6/5} \tag{6}$$

In addition, the time of flight *ToF* of the PSW, defined as the time difference between the arrival of the ISW and the PSW at a given particle location, hereinafter indicated as the sensor particle, can be expressed as [17]:

$$ToF = T_{ti} + T_c + T_{tr} \tag{7}$$

Here, T_{ti} represents the traveling time of the ISW between the sensor particle and the plate interface, T_c represents the contact time between the last particle in the chain and the plate, and T_{tr} is the traveling time of the PSW from the plate interface to the sensor particle.

The traveling times of the ISW and the PSW (T_{ti} and T_{tr} respectively) can be calculated based on the distance between the sensor particle and the plate and their propagation speed. If there are N particles of diameter D between the sensor and the plate, the traveling times of the ISW and PSW is expressed as:

$$T_{ti} = ND/V_i \tag{8}$$
$$T_{tr} = ND/V_r \tag{9}$$

where V_i and V_r denote the speed of the propagation of the ISW and PSW, respectively. The speed of HNSWs propagation (V_s) in an uncompressed granular chain is given by [40]:

$$V_s = 0.9146\, D v_m^{1/5} A^{2/5} m^{-2/5} \tag{10}$$

According to Eq. (10), HNSWs speed (V_s) depends on the diameter (D) and the mass (m) of the particles, the stiffness coefficient of the contact between the particles (A), and the maximum particle velocity (v_m). Chatterjee [71] showed numerically that the maximum particle velocity (v_m) under the propagation of HNSWs is related to the striker velocity (v_{imp}) as: $v_m \approx 0.682 v_{imp}$. Therefore, the traveling times of the ISW and the PSW can be estimated as:

$$T_{ti} = 1.18 N v_{imp}^{-1/5} A^{-2/5} m^{2/5} \tag{11}$$
$$T_{tr} = 1.18 N e^{-1/5} v_{imp}^{-1/5} A^{-2/5} m^{2/5} \tag{12}$$

Additionally, the solution of Eq. (3) provides the dimensionless contact time as a function of the inelasticity parameter, λ [72]:

$$\tau_c = 2.762 + 0.4568 \exp(1.27\lambda) \tag{13}$$

And the interaction time (T_c) is given by:

$$T_c = m^{2/5} v_m^{-1/5} A_p^{-2/5} \tau_c \tag{14}$$

where A_p represents the Hertzian stiffness constant at the particle-plate interface [65]:

$$A_p = \frac{4\sqrt{R}}{3}\left[\frac{\left(1-v_b^2\right)}{E_b} + \frac{\left(1-v_p^2\right)}{E_p}\right]^{-1} \tag{15}$$

The above analytical model only accounts for energy dissipation at the impact by the generation of flexural wave which propagate radially in the plate from the interaction point. However, the model neglects shear deformations in the plate, and energy loss during the impact caused by friction, plastic deformations, and viscous damping at the contact area. Moreover, the analytical model predicts the traveling times of the ISW and the PSW neglecting the initial compression in the chain caused by the weight of the particles in the chain.

3. Results and discussion

3.1. Interaction of HSNWs with pristine and corroded plates

This section presents a comparison of the numerical results relative to a pristine and a corroded steel plate. The plate was 609.6 mm × 609.6 mm × 6.35 mm while the metamaterial supporting the propagation of the wave was composed of nine stainless steel spheres. The plate and the chain particles were made of stainless steel, with the

elastic modulus and the Poisson's ratio were $E = 200$ GPa and $\nu = 0.3$, respectively. Corrosion was simulated by removing a 25.4 mm × 25.4 mm × 5.08 mm coupon below the point of contact between the plate and the chain. Each particle was 19.05 mm in diameter and 28.2 g in mass.

The results are presented in Fig. 2. The left and the right columns refer to the pristine and the corroded plate, respectively. The time history of the displacement of the mass points m_1 to m_8 is shown in Fig. 2a and b. The incident solitary wave was triggered in the chain by applying an initial downward velocity of 0.31 m/s (corresponding to a falling height of 5 mm) to the first particle in the chain (m_1). Consequently, the particles m_1 to m_8 move downward (negative displacement) sequentially as the incident solitary wave propagates through the chain toward the plate interface. Once the wave is reflected back from the chain-plate interface, each particle bounces back to its original rest position. Note that at time equal to 0 μs, each particle exhibits a negative displacement due to the static deformation induced by the weight of the chain. In the corroded plate, this initial deformation and the maximum displacement of the particles m_7 and m_8 are larger than in the pristine plate. Moreover, the time interval between the downward and upward movement of all particles is longer in the corroded plate, i.e., longer impact time and larger time of flight. These differences are caused by the lower contact stiffness at the particle-plate interaction point in the corroded plate.

Fig. 2c and d present the dynamic force at each mass point as the solitary wave propagates through the chain. The force at each particle was calculated by averaging the interaction forces between the particle and the upper and lower adjacent particles, and the contact forces were determined based on the Hertzian contact law and the displacements of the particles, presented in Fig. 2a and b. The averaged interaction forces presented in Fig. 2c and d would be identical to the forces measured by a sensor particle (with embedded PZT) in experiments. The first pulse at each particle represents the ISW and the subsequent pulses represent the PSW and a SSW traveling upward from

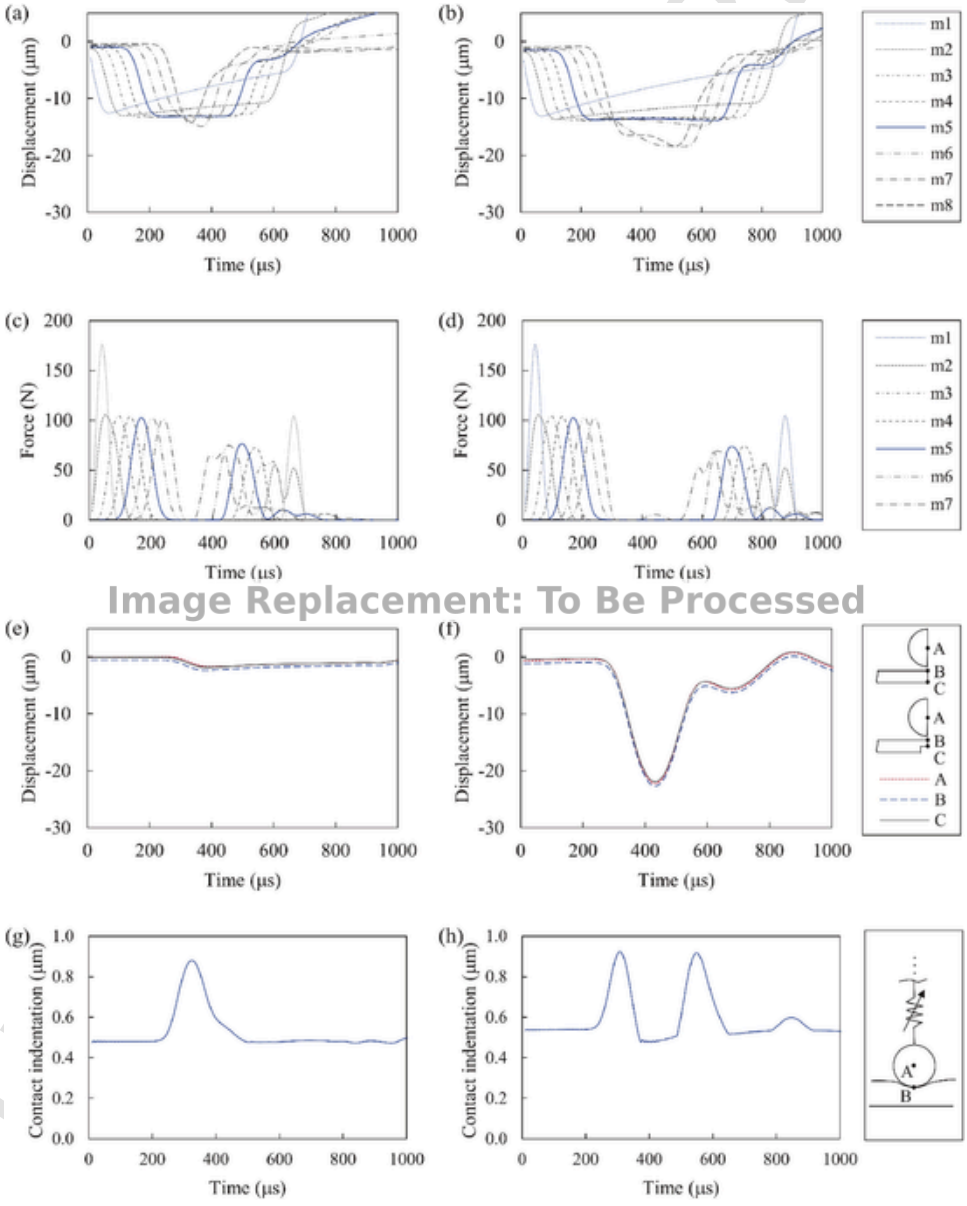

Fig. 2. Numerical results on the interaction of HNSWs with a steel plate in the pristine (left column) and corroded (right column) conditions. (a) andb)] </number> The time history of the displacement of the mass points and (c) and (d) force at the mass points as a solitary wave propagates through the granular chain and interacts with the plate. (e and (f) The time history of the displacement of points A, B, and C, corresponding to the center of the last particle, the contact point in the plate, and the lowest point in the plate below the interaction point. (g and (h)] </number> The time history of the contact indentation at the chain-plate interface.

the chain-plate interface. It should be noted that the crossing of the ISW and PSW at each particle is simultaneous with the movement of the particle downward and upward, respectively. The wave reflected from the corroded plate (Fig. 2d) is weaker and delayed with respect to the wave associated with the pristine plate. This effect can be explained by the lower contact stiffness at the chain-plate interface and larger deflections in the corroded plate (shown in Fig. 2a). The reflected solitary wave is weaker in the corroded plate since more energy is transferred to the plate during the interaction between the last particle and the plate due to the larger deflections in the plate. Furthermore, the corrosion delays the solitary wave because it takes longer for each particle to bounces back to its original position in the corroded plate due to the larger deflections.

The displacements predicted with the FE analysis, including the center of the last particle, the contact point in the plate, and the lowest point (points A, B, and C) in the plate below the interaction point are shown in Fig. 2e and f. The magnitude of the maximum displacements in the last particle and the contact area in the plate are considerably larger in the corroded plate compared to the pristine plate since the contact stiffness decreases significantly in the corroded plate. According to Fig. 2f, as the last particle and the interaction area in the plate reach their maximum displacement (*Time* ≈ 430 μs in the corroded plate), the plate begins to rebound elastically, and the contacting particle is pushed back towards the rest of the chain until it collides with particle m_8 (*Time* ≈ 600 μs in the corroded plate). Consequently, the PSW is induced in the granular chain. Meanwhile, the collision between the contacting particle and m_8 causes the contacting particle and the contact area in the plate to move downward again. Then, the second rebound occurs in the plate (Time ≈ 680 μs in the corroded plates) causing the formation of the SSW in the granular chain. Fig. 2e and f confirm that the lower contact stiffness and the larger deformations in the corroded plate lead to longer delays between the ISW and the PSW.

The contact indentation at the chain-plate interface is also presented in Fig. 2g and h. The contact indentation was obtained by subtracting displacements of point B from the displacement of point A (shown in Fig. 2e and f). In other words, the contact indentation is defined as the difference of the displacements of the contact point in the plate and the center of the interacting particle. According to Fig. 2g, in the pristine plate, the initial elastic indentation caused by the weight of the chain is 0.48 μm. After 220 μs, the incident solitary wave arrives at the interacting particle and presses the particle down toward the plate (refer to Fig. 2e and g). Consequently, the contact indentation increases to a maximum of 0.88 μm at time equal to 325 μs (Fig. 2g). Then, the particle and the plate are bounced back to the original position and the contact indentation decreases to its initial level.

The contact indentation at the interaction of the corroded plate and the particle is shown in Fig. 2h. In this case, the initial elastic indentation due to the chain weight is 0.53 μm. The initial indentation is higher in the the corroded plate than the pristine plate since the contact stiffness between the plate and the interacting particle is lower in the corroded condition. It is shown in Fig. 2f and h that the incident solitary wave arrives at the interacting particle after 220 μs. As the interacting particle is pressed down toward the plate, the contact indentation increases to 0.92 μm at time equal to 310 μs. Then, the particle and the particle's motion slow down as the impact energy is transferred to the plate. As a result, the contact indentation decreases to 0.48 μm at time equal to 370 μs. At time equal to 430 μs, the plate and the interacting particle start to rebound (Fig. 2f), which causes the second phase of contact indentation increasing. The second peak in the contact indentation represent the origin of the PSW created the the chain-plate interface.

In brief, the displacements of the interacting particle and the impact area in the plate are small in the pristine condition (Fig. 2e). Therefore, the chain-plate interaction is fast, and the plate and the particles rebound in a short time (Fig. 2a and g). In contrast, the lower contact stiffness at the chain-plate interface in the corroded condition causes larger displacements in the interacting particle and the impact area in the plate (Fig. 2f). Consequently, the interaction between the chain and plate lasts longer, i.e., the plate and the particles rebound later in the corroded plate. In this case, the extended chain-plate interaction causes two distinct peaks in the contact indentation associated with the ISW and the PSW, respectively.

To quantify the variation of certain solitary wave features, let assume that the sensor particle is in the middle of the chain, i.e., particle #5 in a chain composed of 9 particles, and mass m_5 in the scheme shown in Fig. 1. In this case, the time of flight measured at the sensor particle increases from 328 μs to 378 μs when the 25.4 mm × 25.4 mm × 5.08 mm corrosion exists. In addition, the normalized amplitude of the reflected wave, i.e., the ratio of the PSW amplitude to the ISW amplitude, decreased from 0.74 to 0.57 because of the corrosion.

Fig. 3 compares the numerical results with the results of an experimental study previously conducted by the authors [36]. The numerical results present the time of flight and the normalized amplitude of the reflected solitary wave in a plate containing a localized defect. In this case, the time of flight and the amplitude ratio are plotted as a function of the normalized corrosion depth, defined as the depth of the corrosion defect divided by the initial plate thickness. The normalized corrosion depth varies from 0 to 0.8, i.e., the defect depth varies from 0% to 80% of the initial plate thickness. The experimental results show the same features of the reflected solitary waves in HNSW transducers used to monitor localized corrosion in a plate with similar properties. The data series Experimental 1 and Experimental 2 represent the data recorded in monitoring 50.8 mm × 50.8 mm and 25.4 mm × 25.4 mm corrosion areas, respectively. According to [36], the monitoring process was continued until through-thickness holes were detected in the monitored areas. In Fig. 3, the experimental time of flight and amplitude ratio are plotted as a function of the normalized time, which is calculated as the ratio of the time spent from the start of the corrosion

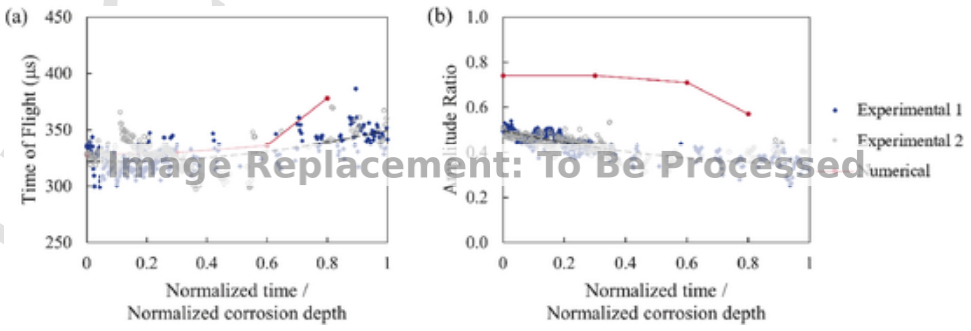

Fig. 3. Comparison of the numerical results and the experimental results reported in [36] on the effect of localized corrosion on (a) time of flight and (b) amplitude ratio. The numerical results present the feature of the reflected solitary waves in contact with a plate containing a localized defect, where the defect depth varies from 0 to 80 percent of the initial plate thickness. The experimental results show the same features of the reflected solitary waves in HNSW transducers monitoring localized corrosions in a plate with similar properties. The dashed line presents the 2nd order regression model fitted to the experimental data.

experiment to the related recording time to the final corrosion time when through-thickness holes were detected. Moreover, the dashed lines present a 2nd order regression model fitted to the experimental data. According to Fig. 3a, the numerical results show a 328 μs time of flight in the pristine condition, i.e., corrosion depth equal to zero. Also, the 2nd order regression model fitted to the experimental data predicts a 320 μs time of flight at the beginning of the test. The experimental observations (scattered data points) show about ± 20 μs error in time of flight around the fitted model due to occasional tilting/vibrations of the sensor disk and stochastic nature of the striker collision [36,73]. However, both the numerical and experimental results show 10-15% increase of time of flight as a localized corrosion progresses in the plate. According to Fig. 3b, the numerical results overestimate the experimental normalized amplitude but both numerical prediction and experimental results estimate about 25% amplitude reduction as corrosion progresses. The overestimation of the numerical amplitude is likely due to an underestimation of energy dissipation in the chain in the numerical model.

3.2. Comparing numerical and analytical results in pristine plates

To quantify the effect of different setup parameters on the propagation of the solitary waves, the numerical and the analytical models described in Sections 2.1 and 2.2 were used to predict the time of flight and the normalized amplitude of the solitary waves as a function of the plate thickness and particles diameter. Fig. 4 shows the two features relative to a chain of nine 19 mm stainless steel particles in contact with plates of different thicknesses. Regardless of the approach, the results show that the time of flight is inversely proportional to the thickness whereas the normalized amplitude is proportional to the thickness. This implies that the dynamic interaction of the last particle in the chain with thinner plates results in a longer contact time and higher energy transfer from the particle to the plate because of the lower contact stiffness at particle-plate interface. For thinner plates, there is a significant difference between the analytical model and the numerical prediction. This difference is because the analytical model does not consider the effect of the plate boundaries on the local contact stresses during the chain-plate interaction. However, the boundary effects on the local stresses are more significant in thin plates. Therefore, the analytical model is less accurate in thin plates. In addition, the analytical model neglects the pre-compression in the chain due to the weight of the particles.

It can be concluded that the numerical model is more comprehensive because it accounts for the effect of the initial compression due to the weight of particles and the effect of plate boundaries in the chain-plate interaction. When compared to the experimental results presented in Fig. 3, the numerical model is closer to the experimental time of flight. As discussed in Section 3.1, the numerical model overestimates amplitude ratio, presumably because the energy dissipation coefficient in the simulated chain was set lower than the actual value.

The effect of the particles' diameter on the time of flight and the normalized amplitude measured at the sensors bead for a 6.35 mm thick plate is shown in Fig. 5. The use of larger particles increases the time of flight because of the increase of the distance traveled by the waves. The normalized amplitude (Fig. 5b) decreases instead with the increase in diameter because of the dependence of the inelasticity parameter on the particles radius. According to Eq. 3, the use of larger particles increases the inelasticity parameter and energy loss at the chain-plate interface. It should be noted that based on Eq. (10), the solitary wave traveling speed increases as the particle size (D) increases, as the stiffness coefficient of the contact between the particles (A) increases, and as the particles mass (m) decreases. Based on Eq. (2), the stiffness coefficient of the contact between the particles (A) is proportional with $D^{-1/2}$. Also, the particles mass is proportional to D^3. Taking all these parameters into account, the solitary wave propagation speed does not depend on the particles size. The fact that time of flight increases as the particle size increases can also be explained based on Eqs. (11) and (12), which show that the traveling times of the ISW and the PSW are proportional to $A^{-2/5}m^{2/5}$ and $e^{-1/5}A^{-2/5}m^{2/5}$, respectively. It can be shown that as the particle size (D) increases, the stiffness coefficient of the contact between the particles (A) increases (Eq. (2)), the particles mass (m) increase, and the inelasticity parameter (λ) increases (Eq. (4)).

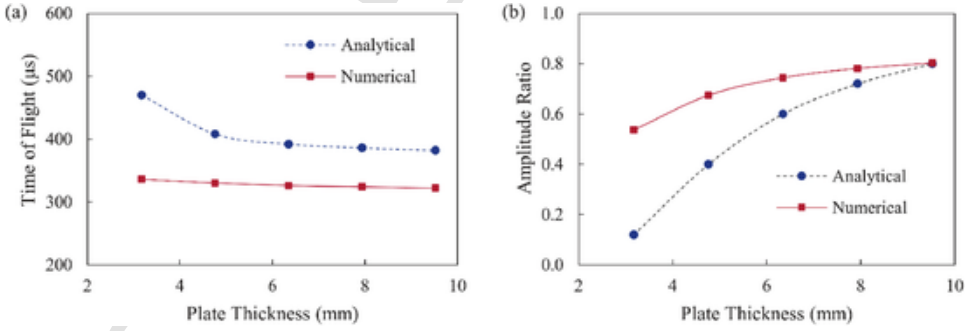

Fig. 4. Numerical and analytical results on the effect of plate thickness on (a) time of flight and (b) amplitude ratio in a HNSW transducer made of 19 mm particles.

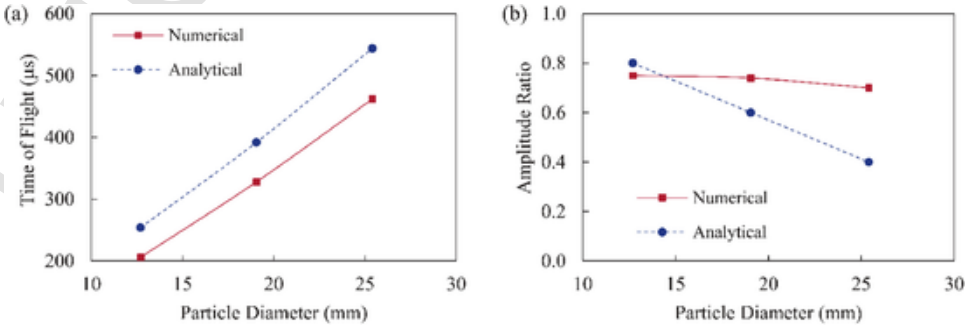

Fig. 5. Numerical and analytical results on the effect of plate thickness on (a) time of flight and (b) amplitude ratio in HNSW transducers in contact with a 6.35 mm thick plate.

Consequently, the restitution coefficient (e) decreases (Eq. (5)), and therefore, the traveling times of the ISW and the PSW increases.

As shown in Fig. 5b, the analytical and the numerical models predict different rates of change in amplitude ratio as the particle diameter varies, causing the two lines to cross each other in the lower diameter region. The difference in slope is likely because of the dissimilarities in modeling the particle-plate interaction in these two methods. As discussed previously, the analytical model neglects local deformations and changes in plate thickness during the particle impact on the plate. In fact, it only takes into account the global bending deformations in the plate. As the particle diameter increases, the bending deformations in the plate increase. Thus, the analytical model predicts that energy restitution factor and amplitude ratio decrease as the particle diameter increase. On the other hand, the numerical model accounts for both the global and local elastic deformation at the chain-plate interface. In other words, the impact energy is partially converted to the kinetic energy of flexural waves propagating in the plate and the strain energy due to local deformations in the plate. As the particle rebounds, the strain energy is converted back to the kinetic energy of the impacting particle leading to higher amplitudes of the reflected solitary waves (in comparison with the analytical model which does not consider the local deformations).

Fig. 6 presents the time of flight and the normalized amplitude measured at the sensor bead as a function of the dimensionless diameter to thickness (D/th) ratio. Two cases of constant diameter and constant thickness were considered. The former includes the results of a solitary wave transducer made of 19 mm spheres in contact with 9.5 mm, 7.9 mm, 6.35 mm, 4.8 mm, and 3.2 mm thick plates (corresponding to a D/th ratio of 2, 2.4, 3, 4, and 6, respectively), and the latter includes the results of solitary wave transducers made of 13 mm, 19 mm, and 25 mm particles in contact with a 6.35 mm thick plate (corresponding to a D/th ratio of 2, 3, and 4, respectively). Fig. 6a shows that the time of flight increases with the increase of D/th. The increase is sharper when the diameter increases and the thickness is kept constant. This suggests that this wave parameter is more influenced by the particles diameter than by the plate thickness. Moreover, Fig. 6b shows that the normalized amplitude decreases with the increase of the dimensionless D/th ratio. In this case, the decrease rate is almost equally affected by either the thickness or the diameter, and the analytical results of the two cases of constant diameter and constant thickness overlap each other perfectly. This is because the inelasticity parameter is non-linearly proportional to D/th ratio (Eq. 4), and the normalized amplitude depends only on the inelasticity parameter (Eqs. 5 and 6).

3.3. Effect of corrosion: a parametric study

To enhance the sensitivity of the proposed NDE method at detecting corrosion at earlier stages, a parametric study was performed using the numerical model described in Section 2.1. Several simulations were performed to quantify how the features of the reflected solitary waves change because a localized 25.4 mm × 25.4 mm corrosion thins the plate underneath the chain. The following variables were considered individually or simultaneously: initial plate thickness, particles diameter, particles Young's modulus, chain length, and sensor bead location.

First, the sensitivity to localized corrosion for different pristine plate thicknesses was investigated and the results are presented in Fig. 7 for five different initial thicknesses, namely 3.2 mm, 4.8 mm, 6.3 mm, 7.9 mm, and 9.5 mm and 20%, 40%, 60% and 80% corrosion depth. Fig. 7 shows that the time of flight increases and the amplitude ratio decreases as corrosion progresses. Also, according to Fig. 7a, the thinner the plate, the higher is the rate of change, i.e. the sensitivity of the proposed NDE method. This effect complies with the analytical model as the inelasticity parameter is inversely proportional to the square of plate thickness (Eq. 4), i.e. energy transfer during the impact increases at a growing rate as the plate thickness decreases. Furthermore, the contact time increases exponentially as the inelasticity parameter increases (Eq. 13). For the two thinnest plates the trend of the amplitude ratio is not monotonic whereas it becomes monotonic for plates 6.3 mm thick or more. For these latter cases, the largest change is observed

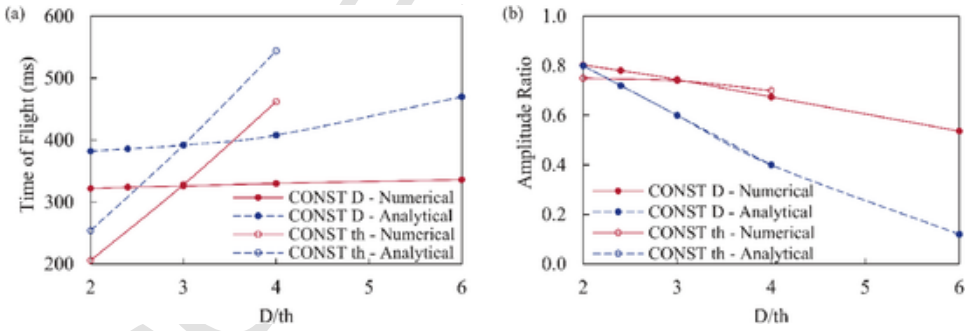

Fig. 6. (a) Time of flight and (b) amplitude ratio as a function of the dimensionless ratio of particle diameter over plate thickness, predicted using the numerical and analytical methods.

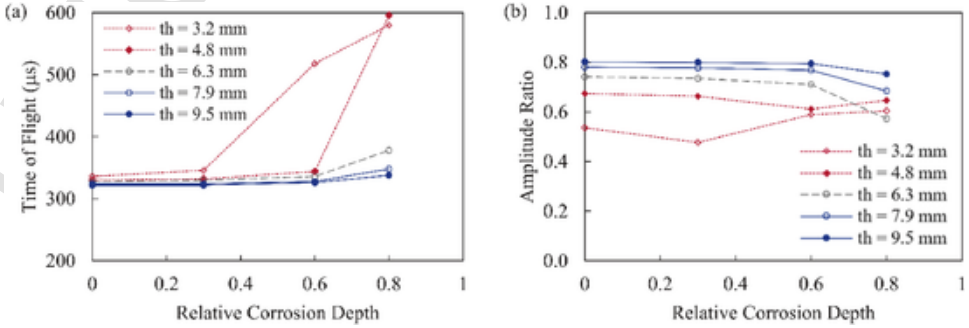

Fig. 7. Effect of plate thickness on the sensitivity of the HNSW-based NDE for the detection of localized corrosion. (a) Time of flight and (b) amplitude ratio as a function of relative corrosion depth in solitary wave transducers in contact with plates with an initial thickness of 3.2 mm, 4.8 mm, 6.3 mm, 7.9 mm, and 9.5 mm.

when corrosion has thinned the plate by more than 60% of the initial thickness. Fig. 7b demonstrates that the amplitude ratio increases in the two thinnest plates as the corrosion relative depth gets higher than 60% or 30%. These data points are related to the case with a remaining thickness of less than 1.3 mm at the monitoring location, i.e., a low contact stiffness at the chain-plate interface. Also, Fig. 7a shows that time of flight increases significantly for these cases, implying a considerably longer contact time between the last particle and the plate. The longer contact time results in the simultaneous upward movement of the plate due to the propagation of flexural waves and the initiation of the reflected solitary waves. Consequently, the kinetic energy of the flexural wave contributes to pushing the last particle back harder and thus causing stronger reflected solitary waves. In brief, the nonmonotonic trend of amplitude ratio in thinner plates can be explained by the propagation of guided waves in the plate.

The effect of the particles diameter on the rate of change of the wave features as a function of corrosion progression is presented in Fig. 8. Three cases were considered, namely solitary wave transducers composed of 13 mm, 19 mm, and 25 mm stainless steel particles in contact with a 6.35 mm thick plate. Monotonic trends were observed for both features and all three diameters: the time of flight increases and the normalized amplitude ratio decreases as corrosion progresses. The largest change is observed between 60 and 80 percent of the corrosion depth. The numerical results show that as a localized corrosion defect progresses in the plate, time of flight increases from 206 μs to 252 μs, from 328 μs to 378 μs, and from 462 μs to 562 μs in solitary wave transducers made of 13 mm, 19 mm, and 25 mm diameter particles, respectively. Therefore, reflected solitary waves are more sensitive to localized corrosion as the particle diameter increases. Besides higher sensitivity, the use of larger particles is advantageous because it creates a larger buffer between the sensor bead and the material to be inspected that could be operating at very high temperature, which would make the use of contact piezoelectric transducers detrimental or impossible.

The sensitivity of the HNSW-based NDE to localized corrosion was also studied in terms of the Young modulus of the beads. Specifically, individual 9-particles chains composed of aluminum, titanium, steel, silicon nitride, and tungsten particles, and in contact with a 609.6 mm × 609.6 mm × 6.35 mm steel plate were considered. Table 1 presents the density, mechanical properties, and thermal conductivity of these materials. The results are presented in Fig. 9a and Fig. 9b for the time of flight and the normalized amplitude, respectively. Fig. 9a shows that time of flight is inversely proportional to the stiffness of the particles. This effect can be explained by observing that the stiffness constant A (Eq. 2) is proportional to the Young's modulus. Therefore, Eq. (10) suggests that the speed of HNSW propagation increases and the traveling times of the ISW and the PSW decrease. Besides, according to Eq. (15), as the elastic modulus of the last particle increase, the Hertzian stiffness constant at the particle-plate interface increases, and interaction time (T_c) decreases (Eq. 14). Although the density and the Poisson ratio of the materials also affect the speed of HNSW propagation and the inelasticity parameter, their effect is smaller when compared to the effect of the Young's modulus. Regardless of the material used, the largest variation of the wave feature is observed after 60% of corrosion. Interestingly, the analysis of the normalized ratio suggests that the heaviest particles significantly enhance the proposed NDE method as both the rate of change is significantly higher than the ones associated with the other four materials taken into consideration in this study. The motivation of such response is associated with the relationship between particles stiffness and inelasticity parameter of the impact, which describes the energy transfer at the impact. If the proposed NDE method is to be employed at high-temperature conditions, chains made of particles with lower thermal conductivity like silicon nitride and titanium should be preferred, as they constitute a thermal buffer that would protect the sensor embedded in the chain.

Another parametric study examined the solitary wave propagation in chains made of 9, 15, and 21 stainless steel 19-mm in diameter particles with the sensor bead located five particles away from the chain-plate interface. The thickness of the plate was 6.35 mm. The results of this analysis are presented in Fig. 10. The numerical data indicate that the length of the granular chain does not affect the features of the reflected solitary wave considerably. Longer chains induce a slightly shorter time of flight (Fig. 10a). This agrees with the fact that more particles induce higher static pre-compression in the chain, which in turn induces higher amplitudes and faster waves. Additionally, according to Fig. 10b, amplitude ratio is slightly higher in longer solitary wave transducers. The reason is that the higher initial static compression in longer chains (due to the particles weight) increases the inelasticity parameter of the impact (Eq. 10). Therefore, based on Eqs. 5 and 6, the coefficient of restitution and the amplitude ratio decreases in longer granular chains. Fig. 10 shows that the effect of the chain length on time of flight and amplitude ratio is insignificant; however, using longer granular chains is advantageous in high-temperature environments since they allow the isolation of the sensor particle from hot zones.

Finally, Fig. 11 shows time of flight and amplitude ratio as a function of relative corrosion depth in a solitary wave transducer composed of 21 particles, where the sensor particle was the 5th, 10th, and 15th particle from the chain-plate interface. As shown in this figure, time of flight decreases if the sensor particle is closer to the inspection medium since the ISW and the PSW travel a shorter distance. On the other hand, amplitude ratio increases if the sensor particle is closer to the inspection medium since a shorter traveling distance of the ISW and PSW causes less energy dissipation of the waves through the chain. Regarding the sensitivity to localized corrosion, numerical results show that the position of the sensor particle does not have a significant effect on the variation rate of time flight and amplitude ratio with respect to the relative depth of the localized corrosion. However, placing the sensor particle further in high-temperature environments is advantageous as it helps to keep the sensor particle away from high-temperature zones.

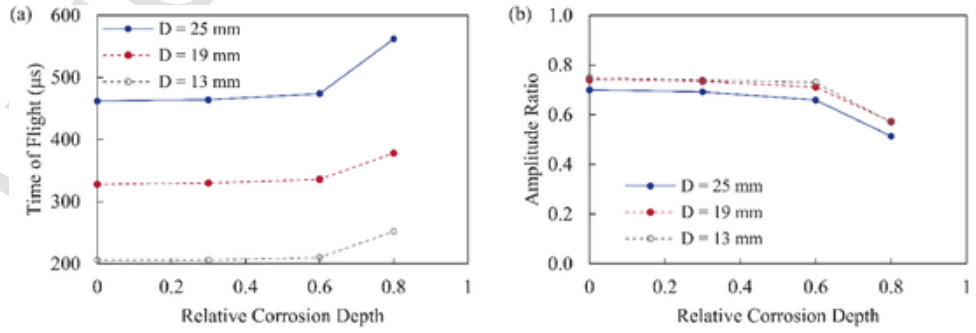

Fig. 8. Effect of particle diameter on the sensitivity of the HNSW-based NDE for the detection of localized corrosion. (a) Time of flight and (b) amplitude ratio as a function of relative corrosion depth in solitary wave transducers composed of 13 mm, 19 mm, and 25 mm particles.

Table 1
Density, mechanical properties, and thermal conductivity of the materials considered in this study.

Material	Material properties			
	Density (kg/m^3)	Young modulus (GPa)	Poisson ratio	Thermal conductivity (W/mk)
Aluminum	2700	70	0.33	205
Titanium	4500	120	0.35	17
Steel	7800	200	0.3	45
Silicon Nitride	3200	280	0.2	10
Tungsten	19600	411	0.27	173

4. Conclusion

In this article, a numerical study about a nondestructive evaluation method based on the propagation and detection of solitary waves is presented. In the framework of the study presented here, the method focuses on the detection of localized corrosion in steel structures.

The numerical results indicate that the HNSW-based NDE method is more sensitive to localized corrosion in thinner plates. Furthermore, it was shown that the method sensitivity improves by using larger, heavier, and stiffer particles. It was also found that the granular chain length and the position of the sensor particle do not affect the properties of the reflected solitary waves significantly. However, in high-temperature environments using longer granular chains and keeping the sensor away from the monitoring object can be beneficial to isolate the vulnerable PZT wafers from hot zones. In addition, the application of granular chains made of silicon nitride particles is advantageous in high-temperature environments since they are relatively stiff and have a lower thermal conductivity that would protect the sensor embedded in the chain. Future studies shall validate empirically the optimal design of the array of periodic particles identified in the study presented in this article.

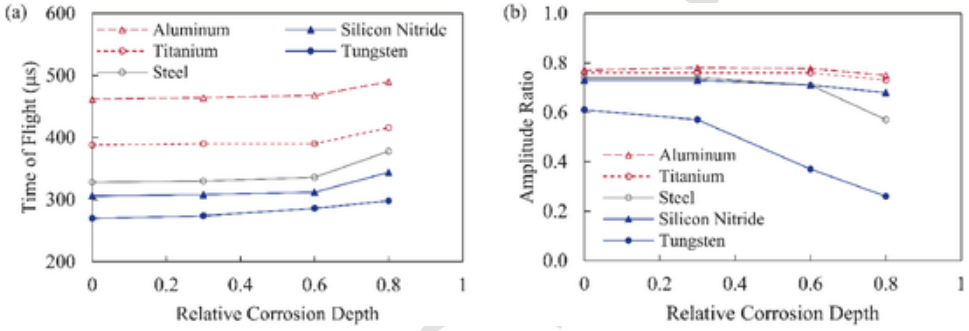

Fig. 9. Effect of particle material on the sensitivity of the HNSW-based NDE for the detection of localized corrosion. (a) Time of flight and (b) amplitude ratio as a function of relative corrosion depth in solitary wave transducers composed of aluminum, titanium, steel, silicon nitride, and tungsten particles.

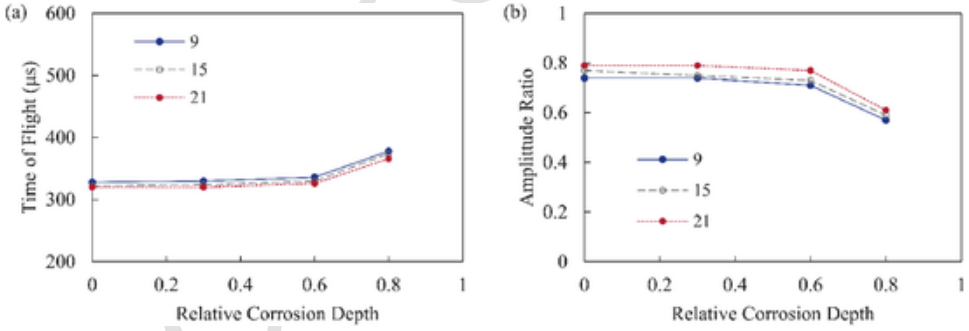

Fig. 10. Effect of chain length on the sensitivity of the HNSW - based NDE for the detection of localized corrosion. (a) Time of flight and (b) amplitude ratio as a function of relative corrosion depth in solitary wave transducers composed of 9, 15, and 21 particles.

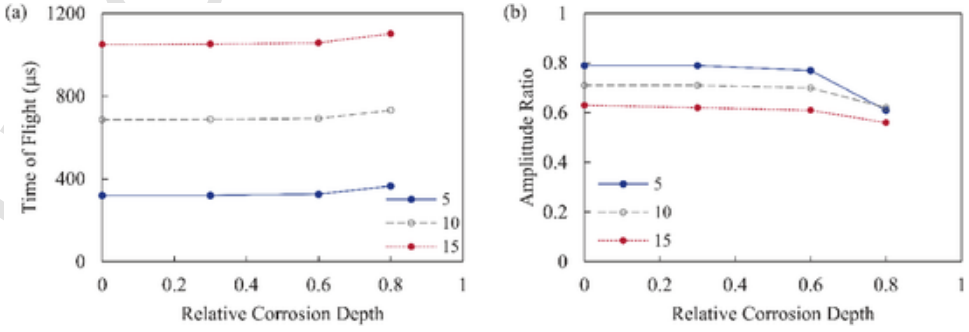

Fig. 11. Effect of sensor location on the sensitivity of the HNSW-based NDE for the detection of localized corrosion. (a) Time of flight and (b) amplitude ratio as a function of relative corrosion depth in a solitary wave transducer composed of 21 particles. The solitary wave force profiles were analyzed at particles #5, #10, and #15.

Declaration of Competing Interest

The authors declare that they have no known competing financial interests or personal relationships that could have appeared to influence the work reported in this paper.

Funding

The work was supported by the U.S. National Science Foundation, Grant No. 1809932, and the American Society for Nondestructive Testing through the 2019 Fellowship Research Award granted to the first author.

References

[1] Daraio C. Energy trapping and shock disintegration in a composite granular medium. Phys Rev Lett 2006;96(5):058002.
[2] Nakagawa M. Impulse dispersion in a tapered granular chain. Granular Matter 2003; 4(4):167–74.
[3] Sokolow A. Absorption of short duration pulses by small, scalable, tapered granular chains. Appl Phys Lett 2005;87(25):254104.
[4] Hong J. Universal power-law decay of the impulse energy in granular protectors. Phys Rev Lett 2005;94(10):108001.
[5] Doney R, Sen S. Decorated, tapered, and highly nonlinear granular chain. Phys Rev Lett 2006;97(15):155502.
[6] Melo F. Experimental evidence of shock mitigation in a Hertzian tapered chain. Phys Rev E 2006;73(4):041305.
[7] Doney RL, Agui JH, Sen S. Energy partitioning and impulse dispersion in the decorated, tapered, strongly nonlinear granular alignment: a system with many potential applications. J Appl Phys 2009;106(6):064905.
[8] Breindel A, Sun D, Sen S. Impulse absorption using small, hard panels of embedded cylinders with granular alignments. Appl Phys Lett 2011;99(6):063510.
[9] Przedborski MA, Harroun TA, Sen S. Localizing energy in granular materials. Appl Phys Lett 2015;107(24):244105.
[10] Spadoni A, Daraio C. Generation and control of sound bullets with a nonlinear acoustic lens. Proc Natl Acad Sci 2010;107(16):7230–4.
[11] Li K, Rizzo P, Bagheri A. A parametric study on the optimization of a metamaterial-based energy harvester. Smart Mater Struct 2015;24(11):115019.
[12] Li K, Rizzo P. Energy harvesting using arrays of granular chains and solid rods. J Appl Phys 2015;117(21):215101.
[13] Li K, Rizzo P. Energy harvesting using an array of granules. J Vib Acoust 2015;137 (4).
[14] Li K, Rizzo P, Ni X. Alternative designs of acoustic lenses based on nonlinear solitary waves. J Appl Mech 2014;(7):81.
[15] Rizzo P, Li K. Analysis of the geometric parameters of a solitary waves-based harvester to enhance its power output. Smart Mater Struct 2017;26(7):075004.
[16] Yang J, Silvestro C, Khatri D, De Nardo L, Daraio C. Interaction of highly nonlinear solitary waves with linear elastic media. Phys Rev E 2011;83(4).
[17] Yang J. Interaction of highly nonlinear solitary waves with thin plates. Int J Solids Struct 2012;49(13):1463–71.
[18] Cai L, Rizzo P, Al-Nazer L. On the coupling mechanism between nonlinear solitary waves and slender beams. Int J Solids Struct 2013;50:4173–83 25-26.
[19] Kim E. Solitary wave-based delamination detection in composite plates using a combined granular crystal sensor and actuator. Smart Mater Struct 2015;24(12): 125004.
[20] Schiffer A, Kim T-Y. Modelling of the interaction between nonlinear solitary waves and composite beams. Int J Mech Sci 2019;151:181–91.
[21] Schiffer A. Interaction of highly nonlinear solitary waves with elastic solids containing a spherical void. Int J Solids Struct 2017;118–119:204–12.
[22] Ni X. Monitoring the hydration of cement using highly nonlinear solitary waves. NDT E Int 2012;52:76–85.
[23] Ni X, Rizzo P. Use of highly nonlinear solitary waves in nondestructive testing. Mater Eval 2012;70(5).
[24] Ni X, Rizzo P. Highly nonlinear solitary waves for the inspection of adhesive joints. Exp Mech 2012;52(9):1493–501.
[25] Singhal T. Weak bond detection in composites using highly nonlinear solitary waves. Smart Mater Struct 2017;26(5):055011.
[26] Yang J, Restuccia F, Daraio C. Highly nonlinear granular crystal sensor and actuator for delamination detection in composite structures. StanfordCA: International workshop on structural health monitoring; 2011.
[27] Schiffer A. Elastic interaction between nonlinear solitary waves in granular chains and composite beams: experiments and modelling. Int J Mech Sci 2020;170:105350.
[28] Yang J. Nondestructive evaluation of orthopaedic implant stability in THA using highly nonlinear solitary waves. Smart Mater Struct 2011;21(1):012002.
[29] Berhanu B, Rizzo P, Ochs M. Highly nonlinear solitary waves for the assessment of dental implant mobility. J Appl Mech 2013;80(1).
[30] Yoon S. Numerical predictions of the interaction between highly nonlinear solitary waves and the microstructure of trabecular bone in the femoral head. J Mech Behav Biomed Mater 2020;103805.
[31] Nasrollahi A, Rizzo P, Orak MS. Numerical and experimental study on the dynamic interaction between highly nonlinear solitary waves and pressurized balls. J Appl Mech 2018;85(3).
[32] Nasrollahi A, Lucht R, Rizzo P. Solitary waves to assess the internal pressure and the rubber degradation of tennis balls. Exp Mech 2019;59(1):65–77.
[33] Nasrollahi A. A nondestructive evaluation approach to characterize tennis balls. J Nondestruct Eval Diagnos Prognos Eng Syst 2019;2(1).
[34] Nasrollahi A, Rizzo P. Axial stress determination using highly nonlinear solitary waves. J Acoust Soc Am 2018;144(4):2201–12.
[35] Nasrollahi A, Rizzo P. Numerical analysis and experimental validation of an nondestructive evaluation method to measure stress in rails. J Nondestruct Eval Diagnos Prognos Eng Syst 2019;2(3).
[36] Jalali H, Rizzo P. Highly nonlinear solitary waves for the detection of localized corrosion. Smart Mater Struct 2020.
[37] Lazaridi A, Nesterenko VF. Observation of a new type of solitary waves in a one-dimensional granular medium. J Appl Mech Tech Phys 1985;26(3):405–8.
[38] Nesterenko V. Propagation of nonlinear compression pulses in granular media. J Appl Mech Tech Phys 1984;(5):24.
[39] Daraio C. Tunability of solitary wave properties in one-dimensional strongly nonlinear phononic crystals. Phys Rev E 2006;73(2):026610.
[40] Nesterenko V. Dynamics of heterogeneous materials. Springer Science & Business Media; 2013.
[41] Sen S. Solitary waves in the granular chain. Phys Rep 2008;462(2):21–66.
[42] Rosas A, Lindenberg K. Pulse propagation in granular chains. Phys Rep 2018.
[43] Chong C. Nonlinear coherent structures in granular crystals. J Phys Condens Matter 2017;29(41):413003.
[44] Khatri D, Ngo D, Daraio C. Highly nonlinear solitary waves in chains of cylindrical particles. Granular Matter 2011;14(1):63–9.
[45] Ngo D. Highly nonlinear solitary waves in chains of hollow spherical particles. Granular Matter 2013;15(2):149–55.
[46] Ngo D, Khatri D, Daraio C. Highly nonlinear solitary waves in chains of ellipsoidal particles. Phys Rev E 2011;84(2 Pt 2):026610.
[47] Zhang W, Xu J. Tunable traveling wave properties in one-dimensional chains composed from hollow cylinders: From compression to rarefaction waves. Int J Mech Sci 2020;191:106073.
[48] Zhang Q. Nonlinear wave scattering at the interface of granular dimer chains and an elastically supported membrane. Int J Solids Struct 2020;46–63 182-183.
[49] Deymier PA. Acoustic metamaterials and phononic crystals. Springer Science & Business Media; 2013 173.
[50] Coste C, Falcon E, Fauve S. Solitary waves in a chain of beads under Hertz contact. Phys Rev E 1997;56(5):6104.
[51] Yoon S. Detection of core-skin disbonds in honeycomb composite sandwich structures using highly nonlinear solitary waves. Compos Struct 2020;256:113071.
[52] Berhanu B, Rizzo P, Ochs M. Highly nonlinear solitary waves for the assessment of dental implant mobility. J Appl Mech 2013;80(1):011028.
[53] Nasrollahi A, Rizzo P, Orak MS. Numerical and experimental study on the dynamic interaction between highly nonlinear solitary waves and pressurized balls. J Appl Mech 2018;85(3):031007.
[54] Nasrollahi A. A nondestructive evaluation approach to characterize tennis balls. J Nondestruct Eval Diagnos Prognos Eng Syst 2019;2(1):011004.
[55] Nasrollahi A, Rizzo P. Axial stress determination using highly nonlinear solitary waves. J Acoust Soc Am 2018;144(4):2201–12.
[56] Misra R. Wireless module for nondestructive testing/structural health monitoring applications based on solitary waves. Sensors 2020;20(11):3016.
[57] Zou F, Cegla FB. High-accuracy ultrasonic corrosion rate monitoring. Corrosion 2018;74(3):372–82.
[58] Gajdacsi A, Cegla F. The effect of corrosion induced surface morphology changes on ultrasonically monitored corrosion rates. Smart Mater Struct 2016;25(11):115010.
[59] Cegla FB. High-temperature 500 wall thickness monitoring using dry-coupled ultrasonic waveguide transducers. IEEE Trans Ultrason Ferroelectr Freq Control 2011;58(1):156–67.
[60] Cawley P. Practical long range guided wave inspection-applications to pipes and rail. Mater. Eval 2003;61(1):66–74.
[61] Heinlein S. Blind trial validation of a guided wave structural health monitoring system for pipework. Mater Eval 2018;76(8):1118–26.
[62] Ghavamian A. Detection, localisation and assessment of defects in pipes using guided wave techniques: a review. Sensors 2018;18(12):4470.
[63] Mariani S, Heinlein S, Cawley P. Compensation for temperature-dependent phase and velocity of guided wave signals in baseline subtraction for structural health monitoring. Struct Health Monit 2020;19(1):26–47.
[64] Ledesma V. Guided wave testing of an immersed gas pipeline. Mater Eval 2009;67 (2):102–15.
[65] Johnson KL, Johnson KL. Contact mechanics. Cambridge university press; 1987.
[66] Shivaraj K, Balasubramaniam K, Krishnamurthy CV, Wadhwan R. Ultrasonic circumferential guided wave for pitting-type corrosion imaging at inaccessible pipe-support locations. J Pressure Vessel Technol 2008;130(2).
[67] Safizadeh MS, Azizzadeh T. Corrosion detection of internal pipeline using NDT optical inspection system. NDT E Int 2012;52:144–8.
[68] Andruschak N, Saletes I, Filleter T, Sinclair A. An NDT guided wave technique for the identification of corrosion defects at support locations. NDT E Int 2015;75:72–9.
[69] Zener C. The intrinsic inelasticity of large plates. Phys Rev 1941;59(8):669–73.
[70] Boettcher R, Russell A, Mueller P. Energy dissipation during impacts of spheres on plates: Investigation of developing elastic flexural waves. Int J Solids Struct 2017; 106:229–39.
[71] Chatterjee A. Asymptotic solution for solitary waves in a chain of elastic spheres. Phys Rev E 1999;59(5):5912.
[72] Müller P. Contact time at impact of spheres on large thin plates. Adv Powder Technol 2016;27(4):1233–43.

[73] Gunkelmann N. Stochastic nature of particle collisions and its impact on granular material properties. Particles in contact. Springer; 2019 565-590.